Impact of Transition Metals and Electrocatalyst Layer Thickness on the Pt-Based Cathodes of Proton Exchange Membrane Fuel Cells – Do Multimetallic Electrocatalysts Necessarily Yield an Improved Performance?

Ricardo Sgarbi, William Aït-Idir, Quentin Labarde, Camille Jourdin, Vincent Martin, Daniele Andreetta, Peizhe Wu, Enrico Negro, Fabio Bassetto, Julia Mainka, et al.

ADVANCED ENERGY MATERIALS
www.advenergymat.de

Impact of Transition Metals and Electrocatalyst Layer Thickness on the Pt-Based Cathodes of Proton Exchange Membrane Fuel Cells – Do Multimetallic Electrocatalysts Necessarily Yield an Improved Performance?

*Ricardo Sgarbi, William Ait Idir, Quentin Labarde, Camille Jourdin, Vincent Martin, Daniele Andreetta, Peizhe Wu, Enrico Negro, Fabio Bassetto, Julia Mainka, Jérôme Dillet, Clémence Marty, Fabrice Micoud, Vito Di Noto, Pawel Kulesza, Olivier Lottin, and Marian Chatenet**

The interplay between i) cathodic electrocatalytic layer (EC layer) features of proton exchange membrane fuel cell (PEMFC), focusing on the oxygen reduction reaction (ORR) electrocatalyst (EC) and the Pt loading; and ii) the PEMFC performance and durability is evaluated. An innovative hierarchical *"core–shell"* carbon nitride multimetallic ORR electrocatalyst (*"PtCuNi/C"* H-EC) is compared with a conventional Pt/C benchmark. The various contributions to PEMFC performance at beginning of test (BOT) are isolated and correlated to the physicochemical features of the ORR EC and the cathodic EC layer. The PEMFC durability is investigated extensively via accelerated stress tests (ASTs) mimicking long-term operation. Particular attention is dedicated to determine how ageing affects: i) PEMFC cell voltage; and ii) the cathode electrochemically active surface area (ECSA). *"Post-mortem"* studies are carried out to probe how ageing influences the cathodic EC layer features, including: i) chemical composition; ii) elements distribution; iii) EC morphology; and iv) structure and crystal size of the Pt-based metal nanoparticles bearing the active sites. Integrating the experimental results allows to identify both the positive and the detrimental effects triggered by the introduction of transition metals (TMs) in the ORR EC on the factors modulating PEMFC performance and long-term operation.

1. Introduction

The *"hydrogen economy"*, wherein hydrogen is the main energy vector, is one of the most promising approaches toward the large-scale practical implementation of the energy transition toward a sustainable future.[1] Fuel cells (FCs) are a family of electrochemical energy conversion devices that are characterized by a very high efficiency, up to two/three-times higher than that of conventional internal combustion engines (ICEs).[2] FCs are a cornerstone of the *"hydrogen economy"*; in particular, proton exchange membrane fuel cells (PEMFCs) are very attractive due to a variety of positive features including a high power density, a low weight per unit mass and a fast start-up time.[3,4] However, to ensure a sufficient performance level and a durability complying with the requirements of practical applications, the electrocatalysts

R. Sgarbi, Q. Labarde, C. Jourdin, V. Martin, M. Chatenet
CNRS
Grenoble INP (Institute of Engineering and Management Univ. Grenoble Alpes)
LEPMI
Univ. Grenoble Alpes
Univ. Savoie Mont Blanc
Grenoble 38000, France
E-mail: marian.chatenet@grenoble-inp.fr

The ORCID identification number(s) for the author(s) of this article can be found under https://doi.org/10.1002/aenm.202403212

DOI: 10.1002/aenm.202403212

W. Ait Idir, P. Wu, J. Mainka, J. Dillet, O. Lottin
LEMTA, CNRS
Université de Lorraine
Nancy 54000, France

D. Andreetta, F. Bassetto
Breton SpA/Electrochemical Division
Via Garibaldi 27, Castello di Godego (TV) 31030, Italy

E. Negro, V. D. Noto
Section of Chemistry for the Technology (ChemTech) and INSTM
Dept. of Industrial Engineering
University of Padova
Via Marzolo 9, Padova (PD) I-35131, Italy

C. Marty, F. Micoud
Univ. Grenoble Alpes
CEA
LITEN
Grenoble F-38054, France

(ECs) promoting the electrochemical processes at the basis of PEMFC operation must still be based on platinum-group metals (PGMs),[5] whose abundance in Earth's crust is extremely limited.[6] Most of the PGM loading in a PEMFC fed with direct hydrogen characterized by a high purity level (e.g., the *"green hydrogen"* obtained by the electrolysis of water powered by renewable energy[7]) is found at the cathode electrode due to the sluggishness of the oxygen reduction reaction (ORR).[8,9] Hence, to devise ORR ECs exhibiting a maximized performance and durability is crucial for a large-scale rollout of PEMFCs toward a practical implementation of the *"hydrogen economy"*.[2]

A very widely explored strategy to raise the intrinsic ORR kinetics of an EC based on PGMs such as Pt, Pd, and Ir is to combine the PGM with one or more transition metal (TM).[10] The most broadly used TMs for this purpose are 3d elements such as Ni, Fe, Co, and Cu.[11] The introduction of TMs in PGM-based ECs is triggering a variety of bifunctional and electronic effects,[12] that ultimately manage to reduce the ORR overpotential by a few tens of mV with respect to conventional ORR ECs based on the corresponding PGM.[10,13–17] On this basis, it is possible to claim that the chemical composition of the nanostructures based on PGMs bearing the ORR active sites has a crucial role to modulate the intrinsic ORR kinetics. In this respect, the role of TMs is critical.

However, it is highlighted that in most cases the scientific papers discussing improved ECs are only concerned to the study of the ORR kinetics and reaction mechanism. Such study is typically carried out by means of highly refined *"ex situ"* experimental techniques, the most popular of which is cyclic voltammetry with the thin-film rotating ring disk electrode (CV-TF-RRDE).[18,19] CV-TF-RRDE can also be used to gauge the durability of an ORR EC by the implementation of suitable accelerated stress tests (ASTs).[16] Yet, the CV-TF-RRDE approach is specifically designed to bypass as much as possible the issues associated with mass-transport, especially at low ORR overpotentials.[19] However, mass-transport may be affected by the details of the distribution of the ionomer on the EC in the cathodic EC layer of a PEMFC.[20,21] Such distribution is modulated by the interactions between the ionomer and the ORR EC, that depend on the latter's surface chemistry (wherein TMs play a crucial role). In the CV-TF-RRDE setup the mass ratio between the EC under investigation attached to the RRDE tip and the support electrolyte wherein the RRDE tip is dipped is negligibly small (on the order of 10^{-6}). Instead, in a realistic PEMFC such ratio is typically larger than 1.[22] Hence, in first approximation measurements carried out by CV-TF-RRDE can ignore the impact of degradation byproducts expelled from the ORR EC upon operation, which include the TMs that can be leached out of multimetallic PGM-based ECs. This is not the case for a *"real"* PEMFC, wherein the ORR EC pollutes the ionomer in the cathodic EC layer with its degradation byproducts during long-term operation, progressively lowering performance.[23,24] On these bases, it is clear that the only way to determine the feasibility of a developmental EC is to implement it at the cathode of a full-fledged PEMFC, to be tested in realistic operating conditions for performance and durability. In summary, the *"ex situ"* experimental approaches typically used in the literature to study PGM-based ORR ECs neglect completely a number of phenomena (e.g., mass-transport and impact of byproducts) that are crucial to set the performance and durability level of a practical PEMFC and that can be affected significantly by the TMs included in such ORR EC.

Over the last 20 years the UNIPD research group proposed an innovative approach for the synthesis of ORR ECs, allowing for a fine control of crucial features of the material such as: i) the chemical composition of the metal nanostructures bearing the active sites; and ii) the morphology of the support.[25–27] A peculiar feature of the ECs obtained by means of the preparation protocol devised by UNIPD is that the support is covered by a nonstoichiometric carbon nitride (CN) layer, where nitrogen is confined on the surface of *"coordination nests"* able to stabilize the metal nanostructures.[25] The best electrocatalysts devised so far by implementing this synthetic approach are *"hierarchical "core-shell" carbon nitride (CN) multimetallic electrocatalysts – H-ECs"* exhibiting the features listed in the following.[25] i) The H-ECs comprise a hierarchical support, including various components playing different roles (e.g., graphene nanoplatelets to better disperse the active sites, together with carbon black to raise electrical conductivity).[28] ii) The support is characterized by a *"core-shell"* morphology, wherein the *"core"* (typically consisting of one or carbonaceous species) is covered by a carbon nitride *"shell"* with a N wt% lower than 5% to minimize the ohmic drops; the *"shell"* surface exhibits by the N- and C-functionalities forming the *"coordination nests"*. iii) The metal nanostructures bearing the ORR active sites are based on a PGM (typically Pt), acting as the *"catalyst"* and yielding most of the ORR performance, together with one or more *"co-catalysts"* (typically first-row TMs such as Ni, Cu, and Co) to boost the ORR kinetics above the PGM baseline. With respect to the traditional approaches pursued to synthesize conventional ORR ECs (e.g., the polyol method and its derivatives)[29,30] the preparation route of UNIPD is characterized by a much larger number of easy-to-modulate synthetic parameters. The latter include: i) the chemicals used to synthesize the precursor of the H-EC; ii) the support; iii) optionally, other templating agents; iv) the details of the pyrolysis process; and v) the activation protocol.[25] It is also very easy to leverage the advantageous properties of innovative components (e.g., advanced carbonaceous supports such as graphene and related materials).[25,28] Hence, a with a single *"general"* preparation route it is straightforward to obtain a multitude of ORR H-ECs exhibiting very diverse, though well-controlled, physicochemical features.[25] The H-ECs can be quite different from conventional state-of-the-art ECs in terms of chemical composition, morphology, and structure.[25]

This work probes the feasibility for practical applications of a H-EC, indicated hereinafter as *"PtCuNi/C"*, by investigating the interplay between: i) its physicochemical features; and ii) the performance and the durability of a PEMFC mounting such H-EC at the cathode. The physicochemical features of PtCuNi/C are studied *"in situ"* upon integration into the cathode of the PEMFC. This goes beyond a conventional fundamental *"ex situ"* study of the ORR kinetics; the investigations carried out herein are focused on the following features of the cathodic catalyst layer (CL): i) the morphology (by means of transmission

P. Kulesza
Faculty of Chemistry
University of Warsaw
Pasteura 1, Warsaw 02-093, Poland

electron microscopy, TEM and scanning electron microscopy, SEM); ii) the chemical composition (through X-ray Energy Dispersive Spectroscopy, XEDS and Inductively Coupled Plasma Mass Spectrometry, ICP-MS); and iii) the long-range structure (adopting Grazing Incidence X-ray Diffraction, GIXRD). The main intent of this work is to elucidate the impact of: i) the transition metals (TMs) included in PtCuNi/C; and ii) the overall Pt loading at the PEMFC cathode on the factors modulating the PEMFC performance (e.g., the contributions to the overall internal resistance) and the PEMFC features associated with durability (e.g., the voltage @ 1 A cm^{-2} and the Roughness Factor of the cathodic EC layer). The resulting information is useful to guide the synthesis of next-generation ORR ECs able to bestow PEMFCs an enhanced performance and durability.

2. Results

The PtCuNi/C H-EC was tested on membrane-electrode assemblies (MEAs) with two different Pt-loadings: 0.1 and 0.3 mg_{Pt} cm^{-2}. These MEAs were electrochemically and physicochemically characterized at the Beginning of Test (BOT) and at End of Test (EOT). The tests refer to a sequence of PEMFC characterizations, initially (BOT), during the Accelerated Stress Tests (AST) and at EOT, as fully detailed in Experimental Section. Two of each cathode catalyst layers (CLs) were produced for i) destructive physicochemical characterization at BOT and ii) tests in unit PEMFC, in which electrochemical performances were measured at BOT and EOT, after which physicochemical EOT characterizations were performed. The MEAs using the PtCuNi/C H-EC were compared to their Pt/C benchmark (Tanaka, 50 wt% Pt, TEC10V50E) counterparts, prepared and characterized similarly, as detailed in a former work of the authors.[31]

2.1. Electrochemical Performance in PEMFC Single Cell

A comprehensive electrochemical evaluation of the PtCuNi/C MEAs performance was obtained by plotting polarization curves, measuring electrochemically active surface area (ECSA) and performing electrochemical impedance spectroscopy (EIS) at BOT and EOT.

Polarization curves at BOT (**Figure 1**, solid lines) exhibit a significant enhancement in cell performance when transitioning from 0.1-PtCuNi/C to 0.3-PtCuNi/C CLs across the entire current density range, including both the low ($j < 0.5$ A cm^{-2}) and high ($j > 1$ A cm^{-2}) current density regions. Similar improvements are observed for benchmark Pt/C CLs, albeit to a lesser extent up to 1 A cm^{-2}, in line with previous findings.[31,32] One also notes that the OCV decreases with the catalyst loading. The anode potential being close to 0 V versus RHE, the OCV is primarily fixed by the cathode potential. The latter is a mixed potential, its value depending on the H_2 cross-over flux (fixed in this study, the membrane is the same in all tests) and the competition between the slow ORR and fast HOR at cathode catalyst (not to speak from the PtO_x/Pt "equilibrium"). Because the ORR is slow and the HOR fast, the cathode potential will naturally be shifted negative at lower Pt loadings (at lower Pt loading, the ORR current is smaller at a given potential than at larger Pt loading). This effect was also clear in Refs. [32,33] This being said, comparing the two highest-loaded cathodes (0.3-PtCuNi/C and 0.3-Pt/C) reveals nearly overlapped activation regions ($j < 0.2$ A cm^{-2}); the polarization plots then irremediably separate at higher current density, the difference being maximal in the mass-transport limiting region ($j > 1.5$ A cm^{-2}). Conversely, the two lowest-loaded cathodes (0.1-PtCuNi/C and 0.1-Pt/C) exhibit significant values disparities throughout the whole cell voltage (and current density) range. In both cases (whatever the cathode catalyst loading), the PtCuNi/C MEAs are outperformed by their benchmark counterparts. The degradation in MEA performance is dependent upon the cathode Pt loadings, being more pronounced for lowest-loaded cathodes (0.1-PtCuNi/C and 0.1-Pt/C), in this case regardless the catalyst composition; the depreciation of performance is greater at high current densities, where activation, ohmic, and mass-transport limitations overlap. This feature is also discernible for the highest-loaded cathode (0.3- PtCuNi/C and 0.3-Pt/C CLs), albeit to a lesser degree. The polarization curves reveal substantial voltage losses between BOT and EOT for all the investigated MEAs, primarily attributed to the decrease of the cathode areal Pt loading and secondarily to the (detrimental) presence of nickel and copper (Figure 1; solid lines versus dotted lines). Figure 1B evidences significant voltage losses at low (0.2 A cm^{-2}) and intermediates (0.6 A cm^{-2}) current densities for both 0.1-PtCuNi/C and 0.1-Pt/C cathodes (the voltage losses are near similar whatever the catalyst nature), reaching very large losses at high current density (1.25 A cm^{-2}). In comparison, the 0.3-PtCuNi/C and 0.3 Pt/C exhibit mitigated voltage losses; although not fully stable, they are more robust than their low-loading counterparts. However, the 0.3-PtCuNi/C cathode performance roughly degrade twice more than the 0.3-Pt/C one, which suggests a deleterious effect of the transition metals (TMs: Ni and Cu). Electrochemical Impedance Spectroscopy data confirm the trend (Figure 1C): the values of the high-frequency resistance (R_{hf}), charge-transfer resistance (R_{ct}), and diffusion resistance (R_d) are all lower at high cathode loading and for the Pt/C versus PtCuNi/C, denoting for a deleterious effect on performance of low-cathode Pt loading and presence of nonnoble transition metals. One will note that Figure 1C shows an increase of the high-frequency resistance when the cathode Pt loading decreases, independently of the nature of the catalyst at stake. This has also been observed in Ref. [34] relative to PEMFC tests with various Pt/C cathode loading all other components being constant (see Table 11 in this earlier reference); this trend was ascribed to the fact that the electrode oxygen transport impedance is inversely proportional to the platinum loading or, equivalently, platinum surface area, and this explanation maintains for the present PtCuNi/C catalyst as well. In addition, the cell potential is not identical at high and low loading and between Pt/C and PtCuNi cathodes. Therefore the heat production and the local temperature within the MEA is also not the same. Lower performance (at given current density, i.e., given water production) induces a higher local temperature and decreases the local RH and the proton conductivity,[35] hence the different HFR.

Figure 2A shows the temporal evolution of the four cell voltages acquired at high current density ($j = 1$ A cm^{-2}) over 24-h intervals during the characterization step of the AST. The cell voltages exhibit a declining trend based on the Pt cathode loading and the presence of nonnoble transition metals in the cathode

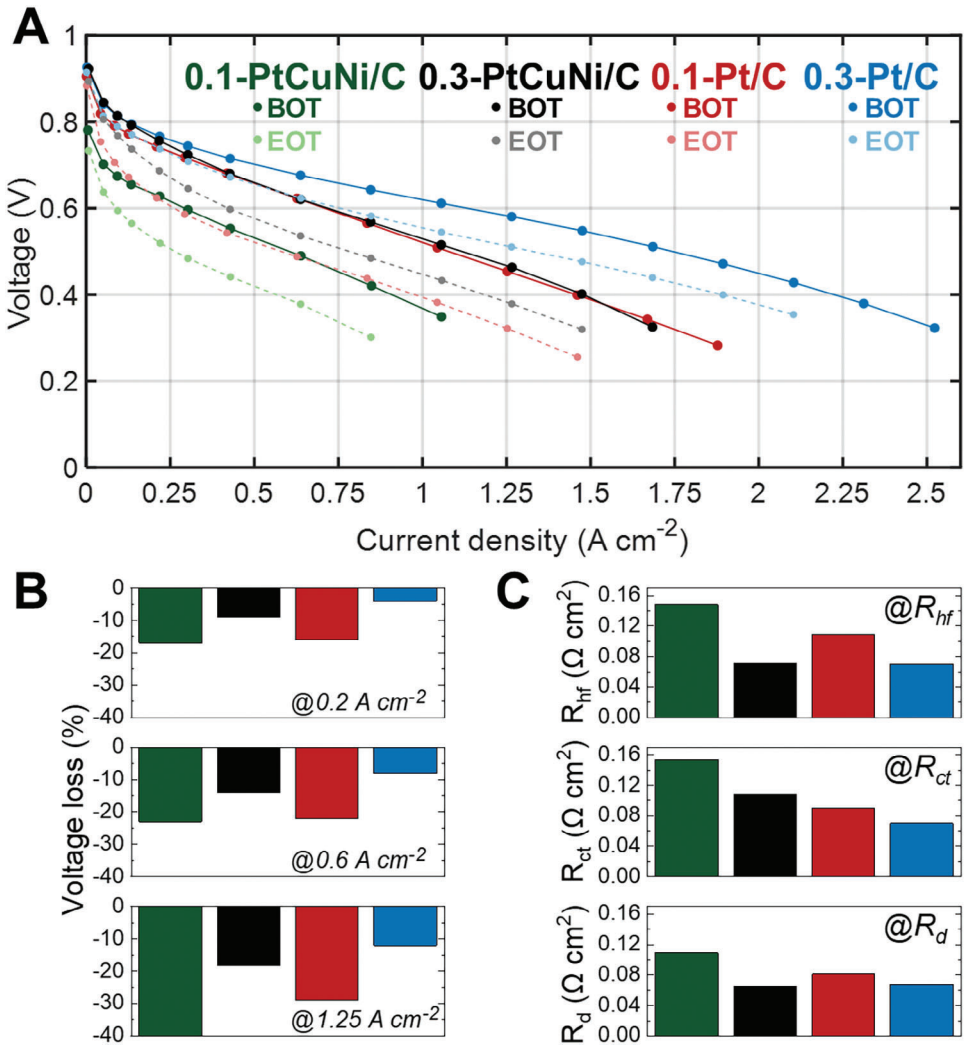

Figure 1. A) Polarization curves for the MEAs comprising 0.1-PtCuNi/C, 0.3-PtCuNi/C, 0.1-Pt/C, and 0.3-Pt/C cathode CLs at BOT and EOT. B) Voltage losses for all investigated MEAs. C) Resistance values obtained at $j = 1$ A cm^{-2} from Electrochemical Impedance Spectra at BOT (details in Figure S1 and Table S1, Supporting Information). R_{hf}: high-frequency resistance, R_{ct}: charge-transfer resistance and R_d: diffusion resistance. 0.1- and 0.3-Pt/C data were reproduced from Ref. [31] with permission from the Royal Society of Chemistry.

CLs up to 288 h, in line with prior data from EIS (Figure S1, Supporting Information) and polarization curve at BOT (Figure 1). Within the initial 48-h interval, a pronounced degradation in cell voltage is discernible, particularly evident for 0.1-Pt/C compared to 0.3-Pt/C (**Table 1**). In contrast, an analysis of degradation rates between 0.1-PtCuNi/C and 0.3-PtCuNi/C reveals that higher Pt-loaded cathodes experience more substantial voltage decay within the same time, possibly attributed to a large degradation kinetics of TMs at low cell voltage (<0.4 V), inducing TM leaching and pollution of the cathode CL ionomer, which is redhibitory to the performance at high current density.[23] The voltage loss rates within the initial 48-h period: 0.1-Pt/C (1933 μV h^{-1}) > 0.3-PtCuNi/C (1585 μV h^{-1}) >> 0.1-PtCuNi/C (691 μV h^{-1}) >> 0.3-Pt/C (368 μV h^{-1}), inversely shifts from 48 h to EOT, reaching a final drop of roughly 50 mV for 0.3-Pt/C and ≥ 100 mV for the other investigated cathode CLs. When voltage drops are measured close to the OCV, they exhibit comparatively lesser magnitudes: 50 mV for 0.1-PtCuNi/C and 10–20 mV for the other CLs; in other words, the CLs that degraded fast in the initial 48 h of AST, degrade much slower after (and inversely).

Table 1. Mean values of cell voltage loss per hour (μV h^{-1}) for 0.1- and 0.3- PtCuNi/C and Pt/C cathodes operated at $j = 1$ A cm^{-2} during the 24 h characterization step (obtained from Figure 2B).

MEA	0.1-PtCuNi/C	0.3-PtCuNi/C	0.1-Pt/C	0.3-Pt/C
BOT < t < 48 h	−691	−1585	−1933	−368
48 h < t < EOT	−176	−89	−16	−151

Figure 2B plots the equivalent ECSA values for the various MEAs. The Pt/C cathodes display higher ECSAs (32 m^2 g_{Pt}^{-1}) at BOT than their TM-containing counterparts: 0.3-PtCuNi/C (25 m^2 g_{Pt}^{-1}) and 0.1-PtCuNi/C (12 m^2 g_{Pt}^{-1}). The Pt/C cathodes experience the two most significant proportional ECSA losses within 48 h (0.1-Pt/C (26%) > 0.3-Pt/C (21%) > 0.3-PtCuNi/C(20%) > 0.1-PtCuNi/C (17%)), which highlights i) that

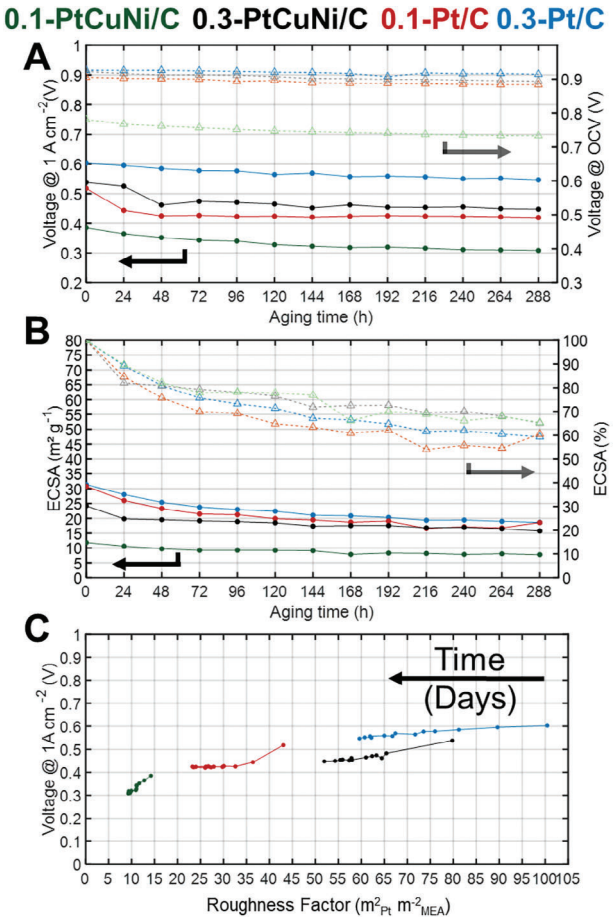

Figure 2. A) Cell voltages (measured at j = 1 A cm^{-2}) during the 24 h-characterization procedure and their OCV along the AST, B) ECSA tracking with its percentage losses. C) Cell voltage (at j = 1 A cm^{-2}) compared to Roughness Factor (RF) measured along the 288 h of ageing test for all investigated cathode CLs. 0.1- and 0.3-Pt/C data were reproduced from Ref. [31] with permission from the Royal Society of Chemistry.

large-roughness cathodes are more subject to ECSA loss (in line with Ostwald ripening that is favored for smaller NPs[36]) and possibly ii) the efficacy of TMs presence in mitigating catalytic area decay (these playing the role of "*sacrificial anode*"[37]), a trend that correlates with voltage losses when comparing the same types of catalyst composition. At EOT, ECSA losses converge to a range between 35% and 40% for all cathodes, with 0.1-PtCuNi/C exhibiting smaller ECSA values (8 m^2 g_{Pt}^{-1}) compared to others (15–20 m^2 g_{Pt}^{-1}), partially accounting for its inferior performance in the polarization curve (Figure 1).

Figure 2C exhibits the cell voltages at j = 1 A cm^{-2} as function of the Roughness Factor (RF) of the cathode, the RF (expressed in m^2_{Pt} m^{-2}_{MEA}) being the product of the cathode Pt loading and ECSA.[38,39] It is noted that the cathode RFs consistently decrease over the 288-h AST, which one can attribute to "classical" degradation (agglomeration, growth, and migration[40,41]) of the Pt-based NPs within the cathode CLs, as discussed further below. In addition, the performance at j = 1 A cm^{-2} basically scales with the roughness factor, in line with Gasteiger's group conclusions:[42] the inferior initial cell performance of 0.1-PtCuNi/C may be attributed to its low RF value, which introduces significant resistance to oxygen transport (see Figure S1, Supporting Information; Figure 1C).[31,34] The fact that the cell voltages at j = 1 A cm^{-2} degrade more for PtCuNi/C cathodes than for Pt/C ones, and more at low Pt-loading than at large one (irrespective of the catalyst composition) not only results from RF decrease, but also from TM leaching and ionomer pollution.[23,24]

Given the utilization of a segmented single PEMFC for the tests, it became feasible to monitor the localized changes in ECSA across all 20 segments along the gas channel.[34,43–45] Segment #1 corresponds to the air inlet at the cathode (H_2 outlet at the anode), while segment #20 corresponds to the air outlet at the cathode (H_2 inlet at the anode). **Figure 3** presents the progression of degradation along the reactant pathway within the channel, as captured by temporal evolution of the local ECSA values for each segment during AST. Whether at BOT (blue curves) or EOT (red curves), the observed fluctuations in local ECSA along the gas channel remain essentially consistent. This suggests that these fluctuations are likely caused by the design of the cell rather than from different cathode Pt-loading/composition, as already observed in Refs. [45,46] (segments near to turns in gas channels exhibit smaller ECSA values[31]). However, the MEA from 0.1-PtCuNi/C exhibits lower ECSA values in segments close to the air inlet (segments 1–4) compared to the average ECSA across the segments near to the air outlet (segments 16–20), which may be caused by its fabrication process (at such low loading, homogeneous elaboration is more delicate: slight decrease/lack of local cathode loading is more impactful in absolute). In addition, the nonuniform distribution of oxygen (air) within the CLs[47] during AST is likely to induce also local variations in temperature and relative humidity,[48,49] thereby exacerbating these fluctuations during AST. Then, different extents of degradation may be observed in the CLs within these segments. Thus, to accurately assess the effect of Pt loading on MEA performance, segments near gas inlets and outlets were deliberately excluded from physicochemical characterizations. Despite these minor biases, these local characterizations do not reveal a significant dependence of local ECSA loss on cathode Pt loading.

2.2. Physicochemical Characterizations

In this section, the MEAs featuring two different PtCuNi/C loadings are subjected to physiochemical characterizations through transmission electron microscopy (TEM), cross section scanning electron microscopy (SEM), X-Ray Energy Dispersive Spectroscopy (XEDS) mapping, Inductively Coupled Plasma Mass Spectrometry (ICP-MS) and grazing-incidence X-Ray Diffraction (GIXRD). The two cathode CLs (0.1-PtCuNi/C and 0.3-PtCuNi/C) are compared to the previous published benchmark 0.1-Pt/C and 0.3/Pt/C.[31] As explained in the previous section, the evaluated regions correspond to segments from 5 to 16, excluding the gas inlet/outlet. It is assumed that this "middle" area of the MEAs do not suffer from any specific local heterogeneities induced by operational conditions or cell design.

The TEM analysis is employed to measure the average sizes of the PtCuNi nanoparticles and their dispersion onto the carbon substrate at BOT and EOT. Representative TEM micrographs (**Figure 4**) of the scraped cathode powder demonstrate uniform

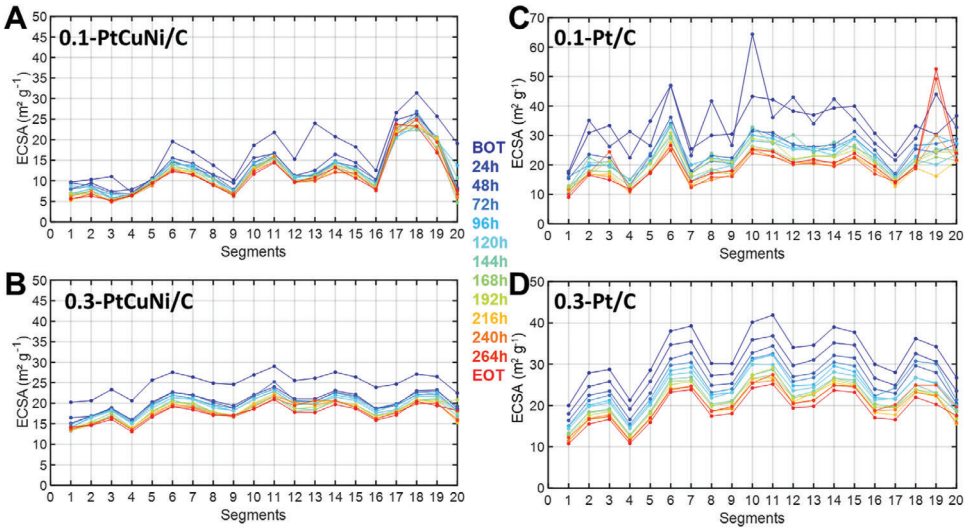

Figure 3. Evolution of local cathode ECSA along the gas channel measured in a segmented cell during the AST for the A,B) PtCuNi/C and C,D) Pt/C cathode CLs. Segment #1: air inlet (cathode) and H_2 outlet (anode); segment #20: air outlet (cathode) and H_2 inlet (anode). 0.1- and 0.3-Pt/C data were reproduced from Ref. [31] with permission from the Royal Society of Chemistry.

distribution of near-spherical PtCuNi nanoparticles on the carbon substrate, with a minor fraction exhibiting agglomeration and/or nonspherical morphology. The mean diameter of isolated and spherical PtCuNi nanoparticles is roughly 4–5 nm, quantified across the two different PtCuNi/C CLs at BOT. In comparison, the mean Pt nanoparticles diameter is slightly smaller for Pt/C CLs (≈3 nm),[31] explaining in part the larger ECSA of the latter CLs noted above. At EOT, the average diameter of the PtCuNi nanoparticles grows to ≈5–6 nm for PtCuNi/C (idem for Pt/C) CLs, concomitant with a widening of the size distribution histograms upon electrochemical ageing. These observations are indicative of the Ostwald ripening mechanism governing Pt nanoparticles growth,[41,50] involving dissolution of smaller nanoparticles (of high surface energy) and re-deposition of the resulting Pt^{z+} ions onto larger nanoparticles. A second nanoparticle growth mechanism happens for adjacent nanoparticles within pre-existing agglomerates, leading to the sintering process (particle coalescence) concurrent with Pt dissolution/re-deposition.[41,51] The effects of these two nanoparticles growth mechanisms are proportionally less intense for PtCuNi/C cathodes than Pt/C ones caused by two factors: i) TMs limit the Ostwald ripening mechanism and/or sintering process[52] and ii) the PtCuNi/C H-EC possess already bigger nanoparticles in its pristine state. In addition, a bimodal nanoparticle size distribution is evident for 0.1-PtCuNi/C that presents region "less degraded" represented as (−) and region "more degraded" represented as (+) in the TEM image and related graph (Figure 4A). It suggests the existence of electrochemically active and inactive regions within this cathode CLs, in line with its higher electrochemical resistance (Figure 1) and smaller/poor ECSA and voltages values than the other CLs.

The cross-sectional morphology of MEAs was examined using SEM to investigate the impact of cathode Pt loadings and Pt-based compositions on MEA performance over AST (**Figure 5**). At BOT, the used ink formulation (Ionomer to Catalyst ratio, I/C = 0.7) and deposition method (blade coating) enabled to maintain a constant composition for all PtCuNi/C MEAs: 44.5 wt% Pt, 1.86 wt% Cu, and 0.2 wt% Ni on carbon substrate. As depicted by orange dotted lines circles in Figure 5A, both PtCuNi/C cathodes exhibit agglomerated ionomer (Nafion) pockets within their CLs at BOT and EOT. These regions may impede the complete CL utilization, leading to smaller ECSA values and cell performance. Also, they may create some electrochemically inactive regions, particularly harsh on thinner CL (0.1-PtCuNi/C), as evidenced by the lowest cell performance (Figure 1) and TEM images (Figure 4A). In the case of PtCuNi/C, this effect appears to be attenuated by the higher Pt-loading in the CL, despite its lower cell performance compared to the 0.3-Pt/C cathode for $j > 0.2$ A cm^{-2} and higher charge-transfer resistance.

At BOT, the increasing cathode Pt (and TMs) loadings led to a proportional increase in cathode CL thickness, as evidenced by SEM micrographs (Figure 5A) and mean cathode CL values derived from two SEM images and regions in Figure 5B. The cathode CL thickness linearly scales with Pt loading, indicating that the porous structure and density of the CL remained relatively constant regardless of areal Pt loading. In contrast, the membrane thickness displayed a slight inverse correlation, with thinner membranes observed at 0.3-PtCuNi/C CLs. It can be hypothesized that thicker cathodes lead to higher membrane compression when the MEA was assembled (Figure 5B shows that the thickest cathode (0.3-PtCuNi/C) compressed the membrane more than the thinnest one (0.1-PtCuNi/C)). These features are independent to the TMs content at the cathode, since similar trends are observed for Pt/C cathode CLs as well.[31] The initial anode thickness displayed a more constant trend, consistent with their catalyst loading: 0.14 and 0.13 mg_{Pt} cm^{-2} for 0.1-PtCuNi/C and 0.3-PtCuNi/C, respectively. At EOT, both cathode CLs exhibited mean thickness values like those at BOT. This suggests that, as expected (see § 4.2), carbon corrosion during AST was not significant enough to induce substantial CO_2 generation associated with CL thinning, even in the presence of nickel and copper, that

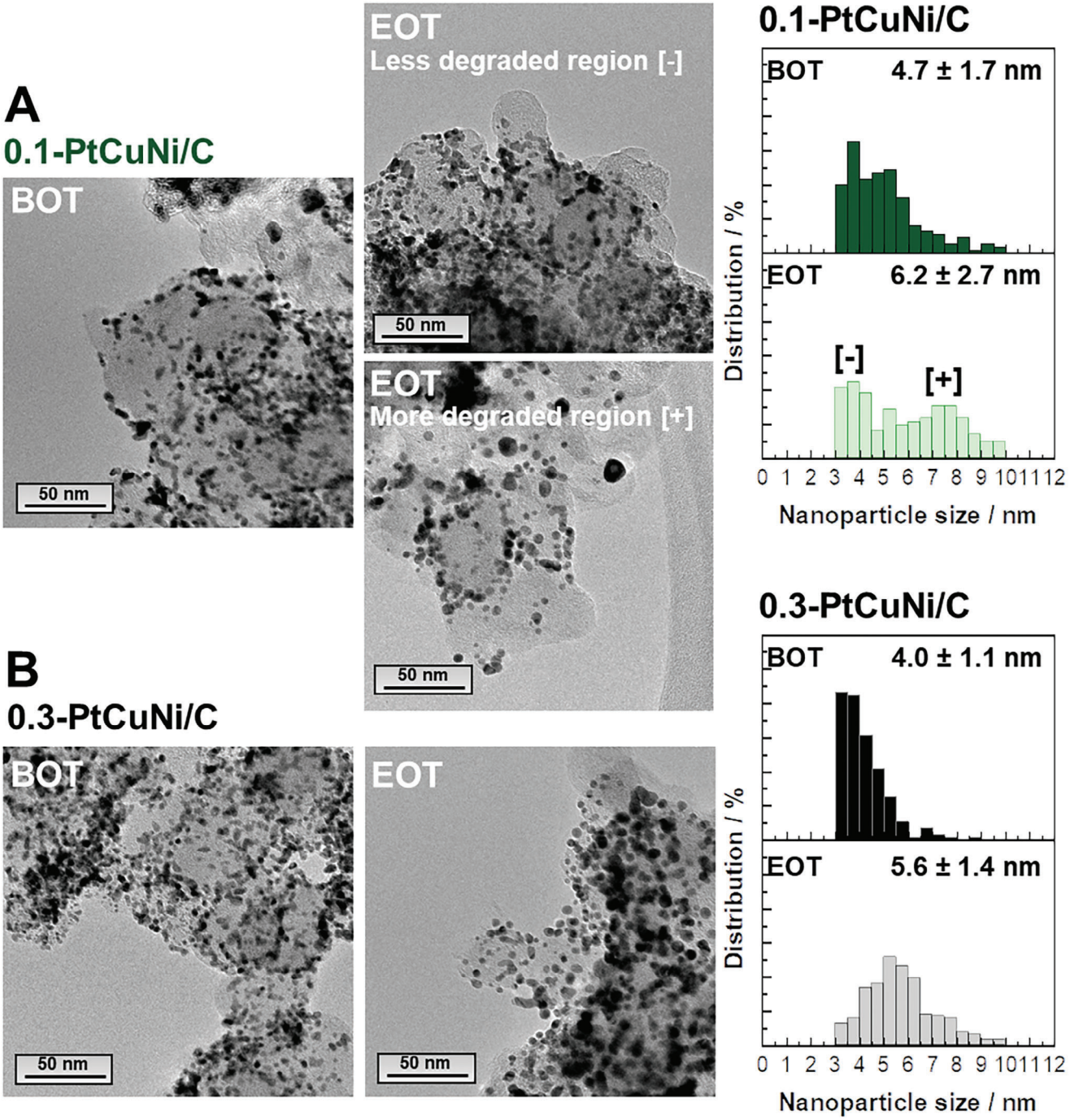

Figure 4. TEM images and corresponding nanoparticle size distribution histograms (comprising the average nanoparticles diameter values) for the (A) 0.1-PtCuNi/C and (B) 0.3-PtCuNi/C cathode CLs at BOT and EOT.

can play the role of sacrificial material, hence possibly limit carbon corrosion.[37,52] The relatively low maximum potential during AST accounts for the minor extent of carbon corrosion, a process being highly dependent on potential.[53]

Active area losses from the cathode of PEMFCs typically arise from three main phenomena: dissolution of Pt nanoparticles into Pt^{2+} ions, subsequent re-deposition in the catalyst layers (resulting in nanoparticle growth via Ostwald ripening and/or electrochemical redeposition), and migration/diffusion of Pt^{2+} ions to the ionomer and the membrane (leading to Pt depletion from the CL). In addition, Pt crystallites may migrate over the carbon support, particularly upon its functionalization or corrosion, resulting in the formation of agglomerated nanoparticles.[40,54] The growth of nanoparticles via Ostwald ripening and their agglomeration were both confirmed through analysis of TEM images, particle size distribution histograms (Figure 4) and ECSA losses

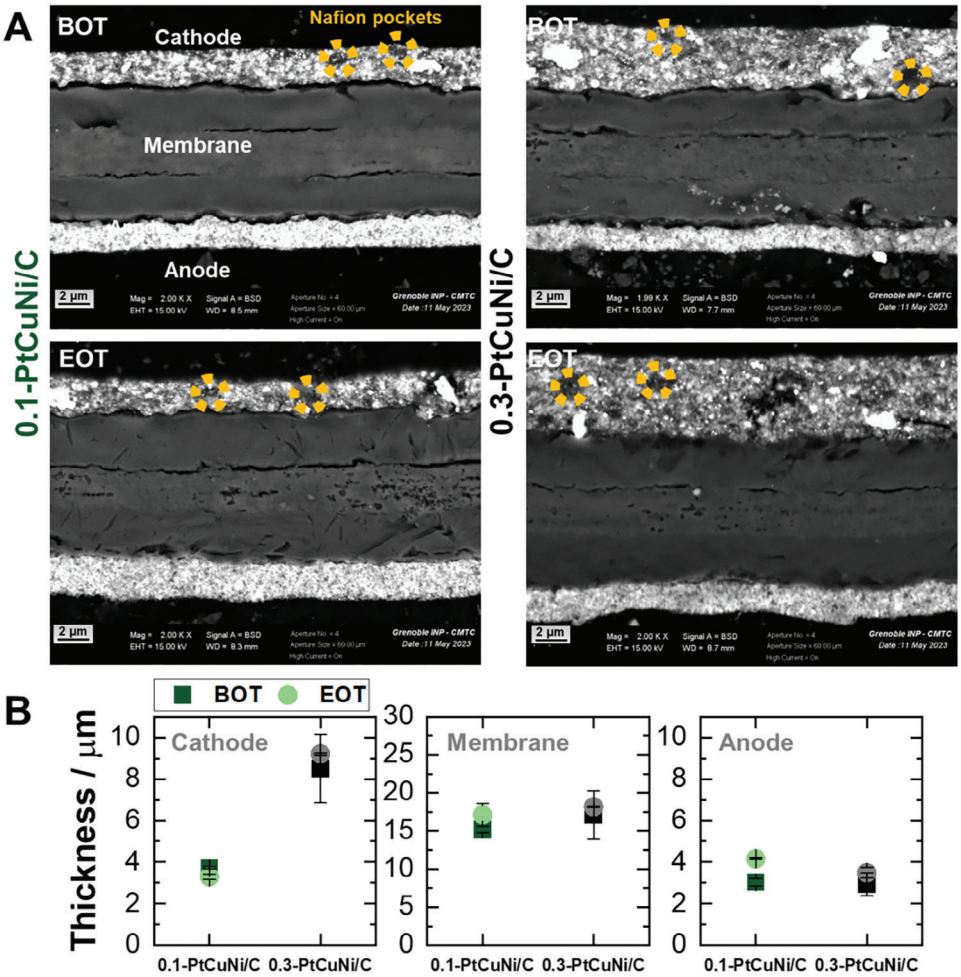

Figure 5. A) SEM images for the MEAs with cathode CLs of 0.1-PtCuNi/C and 0.3-PtCuNi/C at EOT and BOT. B) cathode, membrane, and anode mean thickness values evaluated from two SEM images.

(Figure 2). These effects seem mitigated by the presence of TMs within the cathode CLs, which likely act as "sacrificial metals"[37] owing to their oxophilicity (*i.e.*, oxidation to Metal^{2+}: $E_{oxidation}$ Ni > $E_{oxidation}$ Cu > $E_{oxidation}$ Pt[55]). Thus, the nanoparticles growth and ECSA losses are proportionally less intense for PtCuNi/C than Pt/C. In addition, Pt corrosion and redeposition in the membrane are not discernible on PtCuNi/C CLs, with Pt nanoparticles being retained heterogeneously in the cathode CLs, as evidenced on SEM images and XEDS Pt quantification/mapping at EOT (**Figure** 6A,B). Nickel and copper cannot be detected in the cathode/anode CLs and membrane regions due to their low concentration and the rather high detection limit of the XEDS technique (Figures S2 and S3, Supporting Information). Then, ICP-MS quantification was performed on the scraped catalyst powder from cathode CLs at BOT and EOT. The results show a huge drop in Cu content from gray dotted line to the BOT bar for both PtCuNi cathodes, indicative of significant chemical instability (and leaching) of copper species during the MEA preparation. Cu loss from MEAs slows down over AST procedure compared to the MEA preparation, resulting in leaching of 43% and 18% of residual copper species for 0.1-PtCuNi/C and 0.3-PtCuNi/C, respectively. These features exhibit an increasing trend with increasing CL thickness, due to potential Cu re-precipitation and clustering, particularly evident in thicker CLs. In contrast, complete leaching of Ni species occurs, producing Ni^{2+} species, which may migrate/diffuse toward the air outlet and/or membrane environments (or anode). Ni or Cu nanoparticles creation from these Ni^{2+} or Cu^{2+} species was not detected by SEM-XEDS (Figures S2 and S3, Supporting Information), even in a reducing environment (e.g., H_2 at the anode CL). Such Cu and Ni leaching (and consecutive pollution of the ionomer and membrane by Ni^{2+} and Cu^{2+} cations) elucidates the accelerated degradation of 0.3-PtCuNi/C compared to 0.3-Pt/C observed in polarization curves (Figure 1) and EIS (Table S1, Supporting Information), as well as the poorest performance of 0.1-PtCuNi/C.[23,24]

Grazing incidence XRD measurements were conducted on the PtCuNi/C cathode CLs to detect PtCuNi crystalline phases and monitor phase evolution over the 288-h AST; the crystallite sizes were also calculated. The samples analyzed by XRD equipment was a complete MEA, arranged in the order of cathode (PtCuNi/C H-EC), perfluorosulfonic acid (PFSA) membrane, and anode (Pt/C catalyst), with X-rays incident on the cathode side. This experimental setup, as previously detailed,[31] ensures comprehensive analysis of the cathode CLs while preventing

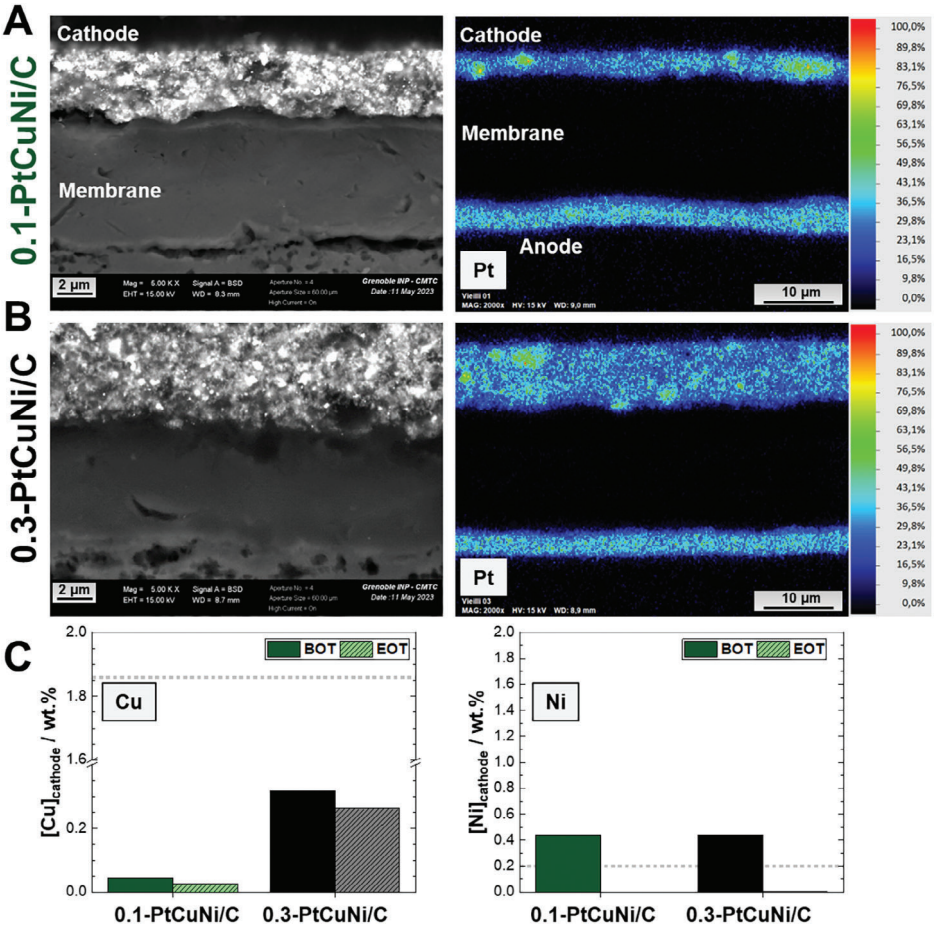

Figure 6. SEM images and XEDS Pt-quantification (mapping) for the MEAs comprising A) 0.1-PtCuNi/C and B) 0.3-PtCuNi/C cathode CLs at EOT. C) Residual copper and nickel concentration in the cathode CLs quantified by ICP-MS at BOT and EOT. The gray lines represent each Cu and Ni concentration in the H-EC powders (before MEAs production).

interference from the anode CLs. The XRD analysis reveals superimposed peaks corresponding to the crystalline phases $Pt_{0.948}Ni_{0.05}$ (PDF 04-017-6800) and Pt_7Cu (PDF 04-021-1092) in the cathode CLs, with pure Cu and Ni phases absent from the diffractograms (**Figure** 7A). The low TMs content (<3 wt%) and the proximity of the Pt-alloys and pure-Pt crystalline phases detected in XRD suggests the presence of pure platinum in their compositions. Furthermore, the XR diffractograms exhibit broader peaks at BOT than at EOT, evidencing growth of the crystallites of the PtCuNi/C H-EC catalyst. The average crystallite sizes ($S_{crystallite}$), determined using the Scherrer equation, are larger (4-5 nm) compared to those obtained for Pt/C (2–3 nm[31]), and they both grow over ageing (PtCuNi/C: 6–7 nm; Pt/C: 4–5 nm), in line with the nanoparticle size statistics obtained by TEM (Figure 4).

Figure 7B provides a magnified view of high-intensity XRD peaks (2θ: from 25 to 50°) with two lines representing the Pt contribution (PDF 00-004-0802) near $2\theta = 40$ and 46°. Initially, both XRD peaks from PtCuNi/C (dark green and black lines) are shifted to higher 2θ values at BOT, indicating different crystalline structures compared to Pt/C (gray perpendicular lines), attributed to the Ni and Cu content. Comparing BOT and EOT, the XRD peaks shift toward Pt contributions (lower 2θ values), reflecting the dealloying process occurring on PtCuNi crystalline phases, consistent with nickel and copper leaching detected by

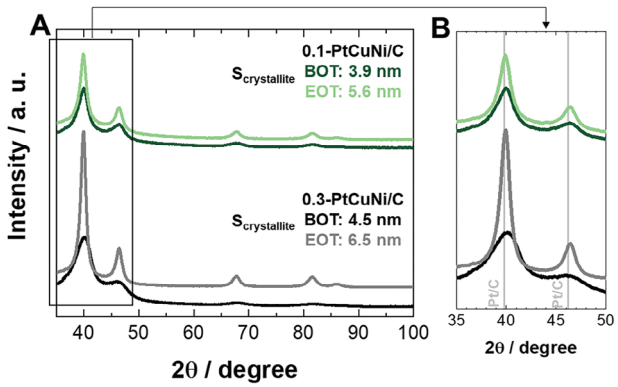

Figure 7. A) Grazing incidence X-ray diffractograms for the 0.1-PtCuNi/C and 0.3-PtCuNi/C cathode CLs at EOT and BOT. B) Highlighted region evidencing that the peak shifts from PtCuNi/C toward Pt/C (gray lines). Crystallite size values calculated at Pt (220) ($2\theta \approx 68$ °).

ICP-MS analyses. Thus, isolated (undetectable by XRD) and/or alloyed TMs nanoparticles are susceptible to leaching from the cathode CLs, regardless their layer thickness, albeit more intense for copper than for nickel in electrochemical environments (Figure 6C).

3. Discussion

The chemical composition of the active sites of an ORR EC, though crucial, is only one of the several factors modulating the performance and the durability of the PEMFC integrating such EC. Indeed, this work shows unequivocally that the formation of a homogeneous cathodic EC layer, wherein the ionomer and the ORR EC are intimately and thoroughly mixed, is also a prerequisite to maximize PEMFC performance. The cathodic EC layer must minimize the prevalence of separate EC and ionomer domains, whose size must be much lower than the thickness of the cathodic EC layer itself (in this work, 2–6 micrometers depending on Pt loading). To achieve such level of homogeneity is increasingly more difficult as the thickness of the cathodic EC layer is lowered (i.e., as the cathode Pt loading is brought from 0.3 to 0.1 mg cm^{-2}). Heterogeneities inhibit the utilization of ECs, yielding the observed ECSA reduction as the cathode Pt loading is lowered. The results presented in this work reveal that the impact of the TMs included in the PtCuNi/C H-EC is twofold.

On the one hand, at BOT the presence of TMs in PtCuNi/C seems to promote the formation of separate EC and ionomer domains. It is hypothesized that this could be ascribed to the hydrophilic character bestowed by TMs to PtCuNi/C, which inhibits the interactions with the hydrophobic PTFE backbones of the Nafion ionomer. The group of Eikerling[56] indeed showed that hydrophilic and hydrophobic catalyst surfaces interact differently with the ionomer, as was also discussed in Ref. [57,58] Herein, this translates in a significantly decreased PtCuNi/C utilization and ECSA from ≈25 to ≈12 m^2 g_{Pt}^{-1} as the cathode Pt loading is brought from 0.3 to 0.1 mg cm^{-2}. No such a dramatic decrease is revealed for PEMFCs mounting the Pt/C reference. All these findings are also consistent with the evidence that in operating PEMFCs R_{hf}, R_{ct}, and R_d increase: i) from Pt/C to PtCuNi/C; ii) as the cathode Pt loading is brought from 0.3 to 0.1 mg cm^{-2}. Indeed, the formation of separate EC and ionomer domains is expected to negatively affect the various charge and mass-transport phenomena that are crucial to minimize the overall PEMFC overpotential, especially at large current density values.

On the other hand, the TMs positively affect the durability of PEMFCs incorporating PtCuNi/C. With respect to Pt/C, the presence of TMs in PtCuNi/C leads to a lower cell voltage loss per hour. This is especially evident for the first 48 h of AST (in the case of 0.1-PtCuNi/C) and between 48 h and EOT (in the case of 0.3-PtCuNi/C). In addition, with respect to 0.1-Pt/C and 0.3-Pt/C, the ECSA of both 0.1-PtCuNi/C and 0.3-PtCuNi/C decreases much more slowly upon AST. These results are interpreted assuming that the TMs would act as a *"sacrificial component"* of PtCuNi/C, being etched selectively during AST due to their higher oxidation potential. This would inhibit the Pt dissolution from the PtM_x nanoparticles bearing the active sites, the first crucial step in several EC degradation mechanisms (e.g., PtM_x growth/agglomeration followed by ECSA reduction). Indeed, upon AST, the grain/crystal size of Pt/C in both 0.1-Pt/C and 0.3-Pt/C as determined by TEM and XRD almost doubles from ≈2.8 to ≈5.5 nm.[31] On the other hand, in the case of 0.1-PtCuNi/C and 0.3-PtCuNi/C the relative increase of grain/crystal size of PtCuNi/C is significantly lower, on the order of 50% (i.e., from ≈4 to ≈6 nm). With respect to 0.3-PtCuNi/C, the Cu content at the cathode of 0.1-PtCuNi/C is much lower. Consequently, the positive effect on PEMFC durability caused by the TM is exhausted quite soon (i.e., in the first 48 h of AST). On the other hand, in 0.3-PtCuNi/C the much larger amount of Cu in the cathodic EC layer ensures that the TM beneficial effect as *"sacrificial component"* lasts much longer up to EOT (i.e., after 288 h of AST). Owing to its low reduction potential and complete etching upon AST, it is expected that Ni does not have a marked impact to improve the durability of PEMFCs mounting PtCuNi/C. Unfortunately, the selective etching of TMs upon operation likely also leads to detrimental effects associated with the poisoning of the ionomer in the cathodic electrocatalytic layer, resulting in higher ohmic drops.

It is widely accepted that the introduction of TMs in PGM-based ECs would typically raise the intrinsic ORR kinetics at BOT.[12] On the other hand, this work highlights that great care must be taken to ensure that the other physicochemical features of ECs including TMs do not inhibit the other phenomena associated with efficient PEMFC operation, especially at high current density (e.g., charge and mass-transport). In this respect the role of TMs may prove detrimental, favoring the formation of heterogeneities in the EC layer and curtailing EC utilization. Even though TMs may act as a *"sacrificial component"* in the ORR EC, thus protecting the nanoparticles bearing the active sites from growth/agglomeration and extending PEMFC durability, they may raise ohmic drops due to the poisoning of the ionomer included in the cathodic EC layer.

4. Conclusion

This work highlights that the design of ORR ECs for PEMFCs able to bestow a performance and a durability beyond the state of the art must take into consideration a large number of factors beyond the mere chemical composition of the active sites. Significant attention must be placed on the role of TMs, to ensure that their beneficial effect on ORR kinetics and durability is not overshadowed by a negative impact on other, equally crucial phenomena such as charge transfer and mass-transport especially upon long-term operation.

On the positive side, the TMs inhibits Pt dissolution from the PtM_x nanoparticles bearing the active sites, acting as a "sacrificial component" of PtCuNi/C. On the negative side, the presence of TMs in PtCuNi/C seems to promote the formation of separate EC and ionomer domains: the hydrophilic character of TMs within PtCuNi/C lowers the interactions with the hydrophobic PTFE backbones of the Nafion ionomer, which negatively affects the various charge and mass-transport phenomena that are crucial to reach large current density values at reasonable cell voltage.

In the light of these findings, further efforts need to be spent to fully reap the potential of the preparation procedure used to obtain PtCuNi/C[59–61] to realize H-ECs able to bestow PEMFCs a performance and durability level beyond the state of the art.

5. Experimental Section

Catalysts and Membrane-Electrode Assemblies (MEAs): The PtCuNi/C H-EC considered in this work was synthesized by BRETON on the basis of a proprietary procedure developed by.[59–61] The details on the synthesis of the PtCuNi/C H-EC that are in the public domain are the following. In the first step, a hierarchical support was prepared by combining suitable carbonaceous species with Cu nanostructured powders. The hierarchical support was then impregnated with a hybrid inorganic-organic precursor comprising Pt, Ni, and an organic binder. The resulting product underwent a multistep pyrolysis process followed by a chemical treatment meant to remove excess inorganic and organic species, thus yielding the final PtCuNi/C H-EC. The assay of Pt, Cu, and Ni in PtCuNi/C was determined by inductively coupled plasma atomic emission spectroscopy (ICP-AES) and is equal respectively to 44.5, 1.86, and 0.2 wt%.

The MEAs used in this study were home-made and based on commercial components except for the cathode catalysts: a reinforced PFSA membrane (MX 820.15 from Gore) and Vulcan carbon (XC72; Cabot) supported Pt nanoparticles from Tanaka (50 wt% Pt, TEC10V50E) in the anode Catalyst Layer (CL). The anode with TEC10V50E and cathode with PtCuNi/C CL inks were prepared respectively in a close manner to a previous work of the authors.[31] Here, the electrocatalyst was mixed with ultrapure water and ethanol with 0.24 ethanol: water mass ratio and the Nafion D2020 solution according to an I/C ratio of 0.7. Then, 3 mm diameter zircon beads were added and the slurry was stirred overnight with a roller mill (IKA roller 10 basic) at room temperature. The inks were finally deposited on an inert PTFE support (250 µm thick) by blade coating the next day. The electrode loading (0.1 or 0.3 mg_{Pt} cm^{-2}) was adjusted by the height of the doctor blade and then controlled afterward by weighing and by X-Ray Fluorescence. In this work, the cathode I/C ratio as well as the ionomer with CL (Nafion D2020) and CL deposition technique were deliberately kept constant, so to produce similar Pt density within CLs cathode loadings. Moreover, the nature of the chosen GDLs (22 BB reference from Sigracet at both anode and cathode sides) was also similar to our previous work with Pt/C cathodes[31] to make meaningful comparison with the PtCuNi/C H-EC.

The catalyst-coated membrane (CCM) was then finalized by decal-transfer of both electrodes onto the membrane using a hot-press at 145 °C under 2 MPa for 180 s using in-house hardware. The GDLs were pressed onto the CCM to form the final MEA using PET gaskets (23 µm) and PTFE seals (150 µm) to control their thickness, reaching ≈20% of compression.

PEMFC Testing Measurements and Durability Protocols: The fuel cell performance measurements and accelerated ageing tests (AST) were identical to those presented in recent work on the influence of platinum loading on MEA durability.[31] The main information is summarized in the following paragraphs.

All measurements were performed using a $5 \times 5 = 25$ cm^2 segmented cell (the same as in Ref. [31]). The anode and cathode plates were machined in 316L stainless steel plate and coated with a thin gold layer to improve the electric contact resistance with the gas diffusion layers. The anode and cathode flow fields are identical with 5 parallel serpentine channels of 0.6 mm in depth, 1 mm in width, and 1 mm ribs. However, the cathode plate was made of 20 electrically insulated segments. These segments allowed independent measurements of the (local) current, impedance and electrochemical surface area (ECSA) to evaluate the homogeneity of the MEA performance and that of the performance degradation rate during the AST.[31,34,43–46] Of course, the total current, global impedance and global ECSA were also measured at the cell scale to check the consistency of the data. Air and hydrogen were supplied to the cell in counter-flow and the cathode segment are numbered so that segment #1 corresponds to the air inlet -and thus H_2 outlet at the anode- and segment #20 corresponds to the air outlet -H_2 inlet- (Figure 3).

During the ageing tests, and during the acquisition of the impedance spectra and of the polarization curves, the cell current intensity was imposed by the electronic load (Armel 0–100A/0–10 V). In the meantime, the measurement of local currents was performed using 20 calibrated shunt resistors of 5 mΩ (i.e., one for each cathode segment). It must be noted that all segments were connected downstream the shunt resistors to allow the measurement of the global cell voltage between the anode and cathode plates (global cell voltage).

To perform the acquisition of the voltammograms and the assessment of hydrogen permeation, the cell was connected to a bipolar power source (Kikusui PBZ-20-20A) to impose positive and negative voltages. The local currents were then measured with the same electronic card (i.e., shunt resistors) as in normal operation while a supplementary 5 mΩ shunt resistance was used to get the overall current.

A multi-stressor AST combining humidity-cycling, Open Circuit Voltage (OCV) hold, and load cycling was chosen to perform. The elementary AST sequence, lasting 105 s, was strictly identical to that performed in the previous work using regular Pt catalyst and active layers[34,43–45] (**Figure 8**). The main idea behind this type of AST is to keep the gas flow rates constant and their inlet humidity at a low or medium value, so that reducing the current (possibly down to OCV) induces dehydration of the cell, and therefore of the membrane.[34,43–45] In this case, the inlet RH of air and hydrogen was set to 50% and their flow rates corresponded to stoichiometries of 4 and 1.5, respectively, at the highest current density (between 0.5 and 1.8 A cm^{-2}, depending on the MEA used). Thus, the stoichiometries increased to very high values when the current density was set to the lowest values (0.02–0.08 A cm^{-2} again, depending on the MEA used) and to infinite values during the 27 s OCV hold at the end of each sequence. The lowest value of the current was set to obtain a cell voltage close to 0.8 V, while the highest value corresponded to ≈0.4 V, these variations inducing a potential cycle sufficient to accelerate the degradation of the cathode materials. However, it should be borne in mind that such AST never leads to high cathodic potential excursions such as those encountered during shutdown and start-up sequences, for example. Consequently, carbon corrosion remains low to moderate. A few second OCV hold was also chosen to include into the AST sequence despite membrane degradation was not targeted in this work: indeed, previous results have shown a considerable increase in electrode degradation when chemical and mechanical stresses are added to load cycling.[34,43–46]

The AST sequence in Figure 8 was repeated for 24 h, 12 times, with a characterization step -lasting ≈2 h- after each 24-h step. The characterization stage is fully described in our previous work.[34,43–45] It included 60 min operation at a constant current density of 1 A cm^{-2}, measurement of the local and global impedance spectra in galvanostatic mode at 1 A cm^{-2}, measurement of the polarization curve, and finally, measurement of the hydrogen permeation current and electrode (anode and cathode) ECSA.

For performance markers, it was considered to measure the performance for three different current densities (0.2, 0.6, and 1.25 A cm^{-2}), that enable to shed light on the so-called activation, intermediate and close to mass-transport regions, respectively and also rely on both polarization plots and electrochemical impedance spectroscopy. It was deliberately chosen not to plot Tafel representation/analysis, Tafel slopes being possibly biased by ohmic and mass-transport effects, as acknowledged in several good practice papers and reviews in the literature.[33,62]

Physicochemical Characterization—Transmission Electron Microscopy (TEM): The catalyst-ionomer powders from 0.1 and 0.3-PtCuNi/C MEAs were carefully scrapped away from uniform areas of the cathode with a razor blade. Then, the resulting powder was mixed in isopropanol and subjected to 10 min of sonication for full ink homogenization; a 10 µL aliquot of the ink was deposited onto a clean Cu-Lacey carbon grid. Analysis of each sample was conducted using a JEOL 2010 transmission electron microscope, operating at 200 kV, and equipped with a LaB_6 filament providing 0.19 nm point-to-point. The nanoparticle size distributions were derived from scrutinizing five distinct TEM images, solely focusing on counting isolated nanoparticles (>200 particles for statistical relevance)

Physicochemical Characterization—Cross-Section Scanning Electron Microscopy (Cross-Section SEM) and X-Ray Energy Dispersive Spectroscopy (XEDS) Mapping: SEM samples of MEAs were prepared by cutting the MEAs (anode/cathode CLs with the membrane) using by a razor blade and embedded in epoxy resin, then polished into an appropriate cross-section SEM sample.[40] The cathode was identified and labeled previously to ensure an easy identification during SEM visualizations. Cross-sectional

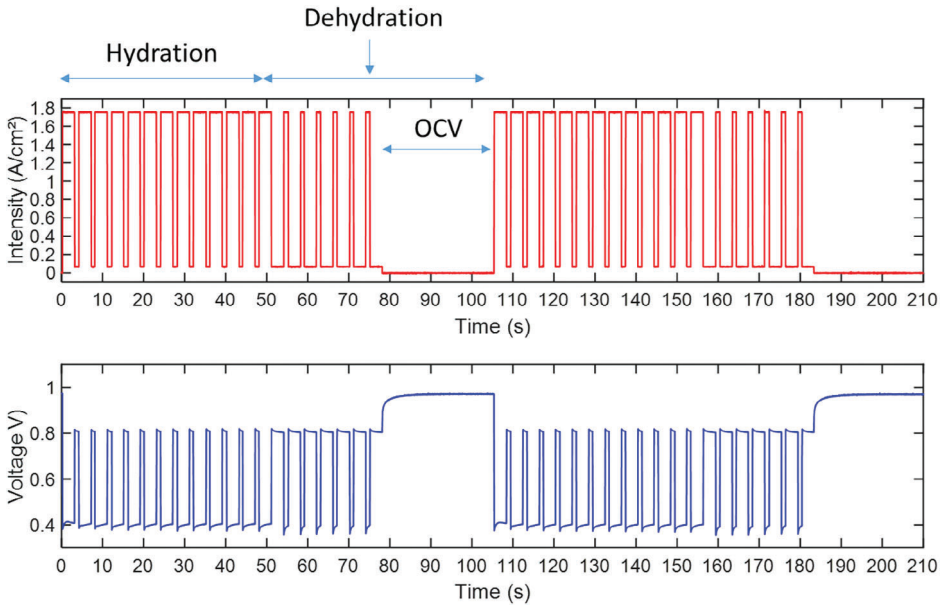

Figure 8. Accelerated Stress Test (AST) – 105 s sequence combining load cycling + humidity cycling + OCV. Dehydration occurs when the duration of the high current sequence is reduced from 3 to 1 s (while that of the low current sequences is increased from 1 to 3 s) and during OCV. The gas flow rates are maintained constant during the whole of the AST, as well as their RH (50%).

SEM imaging was conducted utilizing a field emission gun (FEG) SEM Zeiss Gemini SEM 500 and Ultra 55, both operated at 15 kV electron accelerating voltage in high vacuum conditions. Simultaneously, the XEDS mappings were performed to track the migration of Pt, Cu, and Ni within the MEAs.

Physicochemical Characterization—Inductively Coupled Plasma Mass Spectrometry (ICP-MS): Round-shaped samples (1.54 cm^2) from 0.1- and 0.3-PtCuNi/C cathode CLs were punched at both the Beginning (BOT) and End (EOT) of Test. Then, the catalyst powders were meticulously scrapped away from cathode CLs using a razor blade. Each sample underwent digestion via aqua-regia solution (solution ratio of 1:3 HNO_3/HCl) utilizing a microwave-assisted procedure for 1 h at T = 250 °C to ensure complete dissolution of metal into the solution. Detection and quantification of nickel and copper content were performed using a PerkinElmer NexION 2000 ICP-MS instrument, employing calibration curves established with ICP-MS standard solutions (Carl Roth GmbH & Co.) containing Cu and Ni at concentrations of 0, 5, 10, 20, and 50 µg L^{-1} in 2% HNO_3. All samples were diluted with HNO_3 (Suprapur 68%) and ultrapure water totalizing 2% HNO_3. To account for instrumental drift, 2.5 ppb of Rh (^{103}Rh) was added to each solution. Nickel and copper measurements were conducted across several isotopes (^{58}Ni, ^{60}Ni, ^{63}Cu, and ^{65}Cu) exhibiting similar values, thus confirming the absence of interference and matrix effects under the experimental conditions. Cu and Ni leaching were estimated by subtracting the weight percentage (wt%) metal content between BOT and EOT.

Physicochemical Characterization—Grazing Incidence X-Ray diffraction (GIXRD): The analysis of the crystalline structures in the cathode CLs (with full MEAs) was evaluated on the Rigaku Smartlab X-ray diffractomer operated using the Cu Kα radiation ($\lambda = 0.15\,406$ nm). The measurements were performed from $2\theta = 15$–$120°$ using a scan rate of 1° min^{-1} in an optimized Ω-angle = 0.15°.

Supporting Information

Supporting Information is available from the Wiley Online Library or from the author.

Acknowledgements

R.S., Q.L., C.J., and M.C. thank Stéphane Coindeau and Thierry Encinas for the GIXRD experiments, and Francine Roussel for the SEM images and XEDS mapping/quantification. The research has benefited from the characterization equipment of the Grenoble INP – CMTC platform supported by the Centre of Excellence of Multifunctional Architectured Materials "'CEMAM"' (grant ANR-10-LABX-44-01) funded by the "'Investments for the Future"' Program. This research was funded by European Union EIT Raw Materials ALPE 19247 Project (Specific Grant Agreement No. EIT/RAW MATERIALS/SGA2020/1). This work also received funding under: i) the National Recovery and Resilience Plan (NRRP), Mission 4 Component 2 Investment 1.4 – Call for tender No. 3138 of December 16, 2021 of the Italian Ministry of University and Research, funded by the European Union – NextGenerationEU [Award Number: CNMS named MOST, Concession Decree No. 1033 of June 17, 2022, adopted by the Italian Ministry of University and Research, CUP: C93C22002750006, Spoke 14 "'Hydrogen and New Fuels"']; and ii) the project PERMANENT financed in the framework of the Italian PNRR, M2C2, Investment Line 3.5. J.M., O.L., J.D., W.A.I. and P.W. thank Kévin Mozet from Métro'NRJ LEMTA (Université de Lorraine - CNRS https://lemta.univ-lorraine.fr/).

Conflict of Interest

The authors declare no conflict of interest.

Author Contributions

BRETON and UNIPD elaborated the PtCuNi/C H-EC. C.M. prepared the MEAs. W.A.I. and J.D. performed the PEMFC tests. R.S. performed most physicochemical analyses. R.S. and M.C. drafted the initial version of the MS. UNIPD and P.K. contributed to the conceptualization and final drafting of the MS. All authors contributed to the MS correction.

Data Availability Statement

The data that support the findings of this study are available from the corresponding author upon reasonable request.

Keywords

accelerated stress tests, hierarchical "core–shell" carbon nitride multimetallic electrocatalyst, oxygen reduction reaction, Proton exchange membrane fuel cell, single cell performance, transition metals

Received: July 22, 2024
Revised: November 21, 2024
Published online:

[1] A. Kovač, M. Paranos, D. Marciuš, *Int. J. Hydrogen Energy* **2021**, *46*, 10016.
[2] K. Kodama, T. Nagai, A. Kuwaki, R. Jinnouchi, Y. Morimoto, *Nat. Nanotechnol.* **2021**, *16*, 140.
[3] P. Sgarbossa, G. Crivellaro, F. Lanero, G. Pagot, A. R. Alvi, E. Negro, K. Vezzù, V. Di Noto, in *Electrocatalysis for Membrane Fuel Cells: Methods, Modelling and Applications*, (Eds.: N. Alonso-Vante, V. Di Noto), Wiley, New Jersey, USA **2023**, pp. 227–285.
[4] R. O'Hayre, S. Cha, W. Colella, F. B. Prinz, *Fuel Cell Fundamentals* **2016**, 1.
[5] K. Jiao, J. Xuan, Q. Du, Z. Bao, B. Xie, B. Wang, Y. Zhao, L. Fan, H. Wang, Z. Hou, S. Huo, N. P. Brandon, Y. Yin, M. D. Guiver, *Nature* **2021**, *595*, 361.
[6] P. C. K. Vesborg, T. F. Jaramillo, *RSC Adv.* **2012**, *2*, 7933.
[7] H. Ishaq, I. Dincer, C. Crawford, *Int. J. Hydrogen Energy* **2022**, *47*, 26238.
[8] M. Shao, Q. Chang, J. P. Dodelet, R. Chenitz, *Chem. Rev.* **2016**, *116*, 3594.
[9] V. Di Noto, G. Pagot, K. Vezzù, E. Negro, P. Sgarbossa, in *Electrocatalysis for Membrane Fuel Cells: Methods, Modelling and Applications*, (Eds.: N. Alonso-Vante, V. Di Noto), Wiley, New Jersey, USA **2023**, pp. 69–109.
[10] X. Yang, Y. Wang, X. Tong, N. Yang, *Adv. Energy Mater.* **2022**, *12*, 2102261.
[11] Y. J. Wang, N. Zhao, B. Fang, H. Li, X. T. Bi, H. Wang, *Chem. Rev.* **2015**, *115*, 3433.
[12] Z. Ma, Z. P. Cano, A. Yu, Z. Chen, G. Jiang, X. Fu, L. Yang, T. Wu, Z. Bai, J. Lu, *Angew. Chem. – Int. Ed.* **2020**, *59*, 18334.
[13] E. Antolini, *ACS Catal.* **2014**, *4*, 1426.
[14] A. C. Foucher, D. J. Rosen, S. Yang, D. F. Sanchez, I. Sadykov, D. Grolimund, A. I. Frenkel, C. B. Murray, E. A. Stach, *Chem. Mater.* **2023**, *35*, 4572.
[15] S. Diodati, E. Negro, K. Vezzù, V. Di Noto, S. Gross, *Electrochim. Acta* **2016**, *215*, 398.
[16] T. Wang, A. Chutia, D. J. L. Brett, P. R. Shearing, G. He, G. Chai, I. P. Parkin, *Energy Environ. Sci.* **2021**, *14*, 2639.
[17] K. Oishi, O. Savadogo, *J. Electroanal. Chem.* **2013**, *703*, 108.
[18] F. Dalton, *Electrochem. Soc. Interface* **2016**, *25*, 50.
[19] V. Di Noto, G. Pagot, E. Negro, K. Vezzù, P. J. Kulesza, I. A. Rutkowska, G. Pace, *Curr. Opin. Electrochem.* **2022**, *31*, 100839.
[20] M. Uchida, *Curr. Opin. Electrochem.* **2020**, *21*, 209.
[21] S. A. Berlinger, S. Garg, A. Z. Weber, *Curr. Opin. Electrochem.* **2021**, *29*, 100744.
[22] P. Schneider, A.-C. Scherzer, B. D. Storey, M. Klingele, N. Zamel, D. Gerteisen, *J. Electrochem. Soc.* **2023**, *170*, 104505.
[23] J. Durst, M. Chatenet, F. Maillard, *Phys. Chem. Chem. Phys.* **2012**, *14*, 13000.
[24] B. Kienitz, B. Pivovar, T. Zawodzinski, F. H. Garzon, *J. Electrochem. Soc.* **2011**, *158*, B1175.
[25] V. Di Noto, E. Negro, B. Patil, F. Lorandi, S. Boudjelida, Y. H. Bang, K. Vezzù, G. Pagot, L. Crociani, A. Nale, *ACS Catal.* **2022**, *12*, 12291.
[26] V. Di Noto, E. Negro, *Electrochim. Acta* **2010**, *55*, 7564.
[27] E. Negro, V. Di Noto, *J. Power Sources* **2008**, *178*, 634.
[28] F. Lorandi, K. Vezzù, A. Nale, G. Pagot, Y. H. Bang, E. Negro, V. Di Noto, *J. Power Sources* **2023**, *555*, 232390.
[29] E. I. Santiago, L. C. Varanda, H. M. Villullas, *J. Phys. Chem. C* **2007**, *111*, 3146.
[30] A. R. Corpuz, K. N. Wood, S. Pylypenko, A. A. Dameron, P. Joghee, T. S. Olson, G. Bender, H. N. Dinh, T. Gennett, R. M. Richards, R. O'Hayre, *J. Power Sources* **2014**, *248*, 296.
[31] R. Sgarbi, W. Ait Idir, Q. Labarde, M. Mermoux, P. Wu, J. Mainka, J. Dillet, C. Marty, F. Micoud, O. Lottin, M. Chatenet, *Indus. Chem. Mater.* **2023**, *1*, 501.
[32] P. Schneider, M. Batool, A. O. Godoy, R. Singh, D. Gerteisen, J. Jankovic, N. Zamel, *J. Electrochem. Soc.* **2023**, *170*, 024506.
[33] M. Chatenet, J. Benziger, M. Inaba, S. Kjelstrup, T. Zawodzinski, R. Raccichini, *J. Power Sources* **2020**, *451*, 227635.
[34] W. Aït-Idir, P. Wu, R. Sgarbi, Q. Labarde, S. Touhami, M. Daoudi, A. El kaddouri, J. C. Perrin, J. Dillet, C. Marty, F. Micoud, M. Chatenet, O. Lottin, J. Mainka, *Electrochim. Acta* **2023**, *472*, 143430.
[35] F. Vandenberghe, F. Micoud, P. Schott, A. Morin, C. Lafforgue, M. Chatenet, *Electrochim. Acta* **2025**, *511*, 145364.
[36] P. Wynblatt, N. A. Gjosteis, *Acta Metall.* **1976**, *24*, 1165.
[37] L. Dubau, L. Castanheira, F. Maillard, M. Chatenet, O. Lottin, G. Maranzana, J. Dillet, A. Lamibrac, J. C. Perrin, E. Moukheiber, A. Elkaddouri, G. De Moor, C. Bas, L. Flandin, N. Caqué, *Wiley Interdiscip. Rev. Energy Environ.* **2014**, *3*, 540.
[38] T. A. Greszler, D. Caulk, P. Sinha, *J. Electrochem. Soc.* **2012**, *159*, F831.
[39] X. Sun, H. Yu, L. Zhou, X. Gao, Y. Zeng, D. Yao, L. He, Z. Shao, *Electrochim. Acta* **2020**, *332*, 135474.
[40] E. Guilminot, A. Corcella, F. Charlot, F. Maillard, M. Chatenet, *J. Electrochem. Soc.* **2007**, *154*, B96.
[41] E. Guilminot, A. Corcella, M. Chatenet, F. Maillard, F. Charlot, G. Berthomé, C. Iojoiu, J.-Y. Sanchez, E. Rossinot, E. Claude, *J. Electrochem. Soc.* **2007**, *154*, B1106.
[42] R. K. F. Della Bella, B. M. Stühmeier, H. A. Gasteiger, *J. Electrochem. Soc.* **2022**, *169*, 044528.
[43] T. Gaumont, G. Maranzana, O. Lottin, J. Dillet, S. Didierjean, J. Pauchet, L. Guétaz, *Int. J. Hydrogen Energy* **2017**, *42*, 1800.
[44] S. K. Babu, D. Spernjak, J. Dillet, A. Lamibrac, G. Maranzana, S. Didierjean, O. Lottin, R. L. Borup, R. Mukundan, *Appl. Energy* **2019**, *254*, 113659.
[45] S. Touhami, M. Crouillere, J. Mainka, J. Dillet, C. Nayoze-Coynel, C. Bas, L. Dubau, A. El Kaddouri, F. Dubelley, F. Micoud, M. Chatenet, Y. Bultel, O. Lottin, *J. Power Sources* **2022**, *520*, 230880.
[46] S. Touhami, L. Dubau, J. Mainka, J. Dillet, M. Chatenet, O. Lottin, *J. Power Sources* **2021**, *481*, 228908.
[47] X. Zhang, A. Higier, X. Zhang, H. Liu, *Energies (Basel)* **2019**, *12*, 471.
[48] A. Z. Weber, J. Newman, *J. Electrochem. Soc.* **2006**, *153*, A2205.
[49] Y. Wang, K. S. Chen, J. Mishler, S. C. Cho, X. C. Adroher, *Appl. Energy* **2011**, *88*, 981.
[50] P. J. Ferreira, G. J. la O', Y. Shao-Horn, D. Morgan, R. Makharia, S. Kocha, H. A. Gasteiger, *J. Electrochem. Soc.* **2005**, *152*, A2256.
[51] A. P. Soleymani, L. R. Parent, J. Jankovic, *Adv. Funct. Mater.* **2022**, *32*, 2105188.
[52] F. R. Nikkuni, L. Dubau, E. A. Ticianelli, M. Chatenet, *Appl. Catal. B* **2015**, *176–177*, 486.
[53] T. Drugeot, F. Micoud, E. Pinton, S. Rosini, J. P. Poirot-Crouvezier, L. Poupin, Y. Bultel, *Int. J. Hydrogen Energy* **2022**, *48*, 5630.

[54] P. C. Okonkwo, O. O. Ige, E. M. Barhoumi, P. C. Uzoma, W. Emori, A. Benamor, A. M. Abdullah, *Int. J. Hydrogen Energy* **2021**, *46*, 15850.
[55] W. M. Haynes, D. R. Lide, T. J. Bruno, in *Handbook of Chemistry and Physics: A Ready-Reference Book of Chemical and Physical Data*, CRC Press, Boca Raton **2017**.
[56] K. Malek, T. Mashio, M. Eikerling, *Electrocatalysis* **2011**, *2*, 141.
[57] M. Tempelaere, M. Zimmermann, M. Chatenet, *Curr. Opin. Electrochem.* **2023**, *41*, 101353.
[58] M. Chatenet, S. Berthon-Fabry, Y. Ahmad, K. Guérin, M. Colin, H. Farhat, L. Frezet, G. Zhang, M. Dubois, *Adv. Energy Mater.* **2023**, *13*, 2204304.
[59] V. Di Noto, E. Negro, A. Bach Delpeuch, F. Bertasi, G. Pagot, K. Vezzu, Graphene and Other 2D Materials as Layered "Shells" *Supported on "Core" Nanoparticle Carriers*, **2018**.
[60] V. Di Noto, E. Negro, K. Vezzu', F. Bertasi, G. Nawn, L. Toncelli, S. Zeggio, F. Bassetto, Electrocatal. Carbonitride Matrices, **2017**.
[61] L. Toncelli, S. Zeggio, F. Bassetto, M. Casarin, V. Di Noto, E. Negro, A. Nale, H. Bang Yannick, K. Vezzu', G. Pagot, Method and Plant for Activating Catalyst, *Patent WO2021064662A1* **2021**.
[62] M. Chatenet, B. G. Pollet, D. R. Dekel, F. Dionigi, J. Deseure, P. Millet, R. D. Braatz, M. Z. Bazant, M. Eikerling, I. Staffell, P. Balcombe, Y. Shao-Horn, H. Schäfer, *Chem. Soc. Rev.* **2022**, *51*, 4583.